Supporting Information

Spatiotemporal Spectroscopy of Fast Excited-State Diffusion in 2D Covalent Organic Framework Thin Films

Laura Spies[1#], Alexander Biewald[1#], Laura Fuchs[2], Konrad Merkel[2], Marcello Righetto[3], Zehua Xu[1], Roman Guntermann[1], Rik Hooijer[1], Laura M. Herz[3,4], Frank Ortmann[2], Jenny Schneider[1], Thomas Bein[1], Achim Hartschuh[1*]*

[1]Department of Chemistry and Center for NanoScience (CeNS), University of Munich (LMU), Butenandtstraße 5-13, 81377 Munich, Germany

[2]TUM School of Natural Sciences, Department of Chemistry, Technische Universität München, 85748 Garching, München, Germany

[3]Clarendon Laboratory, University of Oxford, Department of Physics, Oxford OX1 3PU, UK

[4]Institute for Advanced Study, Technische Universität München, Lichtenbergstr. 2a, 85748 Garching, München, Germany

Table of Contents

Table of Figures

S1. Materials and Synthesis

All solvents were purchased from *Sigma Aldrich*, *Acros* or *TCI Europe* in the common purities *purum*, *puriss* or *reagent grade*. The materials were used as received without additional purification and handled in air unless otherwise noted. *N,N,N',N'*-tetra(4-aminophenyl)benzene-1,4-diamine **W** was purchased from Carbosynth/BLDpharm. Benzo[1,2-b:4,5-b']dithiophene-2,6-dicarboxaldehyde **BDT** was synthesized according to the literature.[1]

COF bulk material was synthesized according to our prior report in an Argon filled glove box.[2] In a culture tube, a solid mixture of W (0.013mmol, 6 mg) and BDT (0.025 mmol, 6.26 mg) was suspended in 1 mL mesitylene and benzyl alcohol (500 µL each). Subsequently, 50 µL of acetic acid (aqueous, 6 M) was added. The culture tube was tightly sealed and heated at 100 °C for 72 h. The resulting dark red suspension was filtrated hot and the isolated powder thoroughly washed with THF (~10 mL). The obtained red powder was dried under vacuum, followed by extraction in supercritical CO_2 at 110 bar and 40 °C for 1 hour.

COF thin films were synthesized according to our prior report in autoclaves equipped with a teflon liner holding the substrate in a horizontal position.[2] Glass and quartz substrates were cleaned in detergent solution (Hellmanex III, 1% *v/v*, water, acetone and isopropanol). The substrate was immersed into a suspension of W (2.5 µmol, 1.2 mg) and BDT (5 µmol, 1.25 mg) in 2 mL mesitylene and benzyl alcohol (v:v 1:1) and 100 µL of acetic acid (aqueous, 6 M). The autoclave was sealed under Argon and heated at 100 °C for 1 day. After cooling to room temperature, the COF film was rinsed with dry THF and dried under reduced pressure. **Unoriented COF thin films** were grown on an SiO_2 inverse opal structure. The inverse opal structure was grown on a glass substrate following a published procedure.[3] In order to grow an unoriented film with comparable thickness on top of the substrate and account for the COF material growing within the inverse opal structure, the amount of precursor for the film synthesis was increased to 6 mg (12.5 µmol) and 6.25 mg (25 µmol) for W and BDT, respectively. The synthetic procedure remained unchanged.

S2. Methods

2D grazing-incidence wide angle X-ray scattering (GIWAXS) data were recorded with an Anton Paar SAXSpoint 2.0 system equipped with a Primux 100 micro Cu K_α source and a Dectris EIGER R 1M detector. The oriented (unoriented) COF films were positioned at a sample-detector distance of 140 mm (156 mm) and were measured with an incidence angle of 0.2° (0.3°).

Powder X-ray diffraction (PXRD) measurements were performed using a Bruker D8 Discover with Ni-filtered Cu K_α radiation and a LynxEye position-sensitive detector.

Scanning electron microscopy (SEM) micrographs were obtained with an FEI Helios NanoLab G3 UC microscope equipped with a Schottky field-emission electron source operated at 1 – 30 kV.

Transmission electron microscopy (TEM) was performed on a FEI Titan Themis instrument equipped with a field emission gun operated at 300 kV.

Nitrogen Sorption isotherms were recorded with Quantachrome Autosorb 1 and Autosorb iQ instruments at 77 K. The sample was outgassed for 24 h at 120 °C under high vacuum prior to the measurements. Pore size distributions were calculated using the QSDFT model with a carbon kernel for cylindrical pores.

UV-Vis-NIR spectra were recorded on a Perkin-Elmer Lambda 1050 spectrometer equipped with a 150 mm integrating sphere, photomultiplier tube (PMT) and InGaAs detectors. **Diffuse reflectance spectra** were collected with a Praying Mantis (Harrick) accessory and were referenced to barium sulfate powder serving as 100 %R standard. The specular reflection of the sample surface was removed from the signal using apertures that allow only light scatter at angles > 20° to pass.

The **structure model** of the WBDT COF was constructed using the Accelrys Materials Studio software package, applying a P1 symmetry. The structure model was optimized using the Forcite module with the Universal force-field. Structure refinements using the Pawley method were carried out using the Reflex Powder Refinement module of the Materials Studio software.

Atomic force microscopy was measured using a NANOINK AFM setup. A standard tapping mode silicon AFM tip from NANO WORLD was used. The tip diameter was 20 to 40 nm and the force constant of the cantilever was ~42 N/m (length = 125 µm, resonance frequency ~330 kHz). All measurements were performed in tapping mode.

Confocal photoluminescence measurements. For photoluminescence (PL) measurements, hyperspectral images and time-resolved PL images, a home-built confocal laser scanning microscope was used. It is based on a microscope body (NIKON) which is combined with a *xyz*-piezo-scanning stage (PHYSIK INSTRUMENTE) for the room temperature (RT) measurements. Herein, the samples are measured upside down in epi-direction using an oil immersion objective with 1.4 NA (NIKON). All

low temperature (LT) measurements were performed on a self-built microscope with a commercial cryostat system from ATTOCUBE including scanner, positioner, vacuum chamber and pumps and the cooling apparatus. The microscope around this system is self-built and uses a long-working-distance objective with 0.75 NA (ZEISS). Both microscopes are connected to the same detection path. A beamsplitter (MELLES GRIOT 03BTL005 for RT-setup, THORLABS BSW29R for the LT-setup) and a spectral 490 or 550 nm long pass filter is used to separate the laser from the PL-light. A sub picosecond laser (ichrome TOPTICA) tunable from 476 nm to 645 nm is used for excitation. Here, the excitation wavelengths of 476 nm and 510 nm laser light are additionally filtered by a 473/10 nm (CHROMA) or 510/10 nm (THORLABS) band pass respectively, which is positioned in the excitation arm. The detection side consists of two parts, which are separated by a rotatable mirror. Additionally, a tiltable mirror in the back focal plane is installed for the diffusion measurements scanning around the confocal spot. One arm in the detection has an avalanche photo diode (APD, type: MPD PDM, detector size 50 x 50 µm), which can be combined with Time Correlated Single Photon Counting (TCSPC) electronics (BECKER UND HICKEL) measuring time-resolved PL transients. The second part consists of a spectrometer (ANDOR SHAMROCK SRi303) combined with an open electrode CCD camera (ANDOR NEWTON DU920) recording spectra. The data are recorded using a customized LABVIEW (NATIONAL INSTRUMENTS) program that combines the manufacturers' software with our desired measurements. Further processing and analysis are carried out using MATLAB (MATHWORKS) to obtain the PL spectra, TCSPC transients and the images.

S3. WBDT bulk powder characterization

Characterization of the bulk powder of WBDT COF was conducted including PXRD, FTIR, nitrogen sorption, steady-state PL and UV-Vis spectra as well as SEM measurements. PXRD of the WBDT COF shows distinct reflections at $2\theta = 2.00°$, 3.50°, 4.04°, 5.38°, 6.11°, 7.36°, 8.14°, 8.96°. Using the Materials Studio software package, Pawley refinement of the PXRD was conducted, assuming P1 symmetry and yielding the unit cell parameters, with $R_{wp} = 4.20\%$ and $R_p = 3.40\%$ (**Figure S1**).

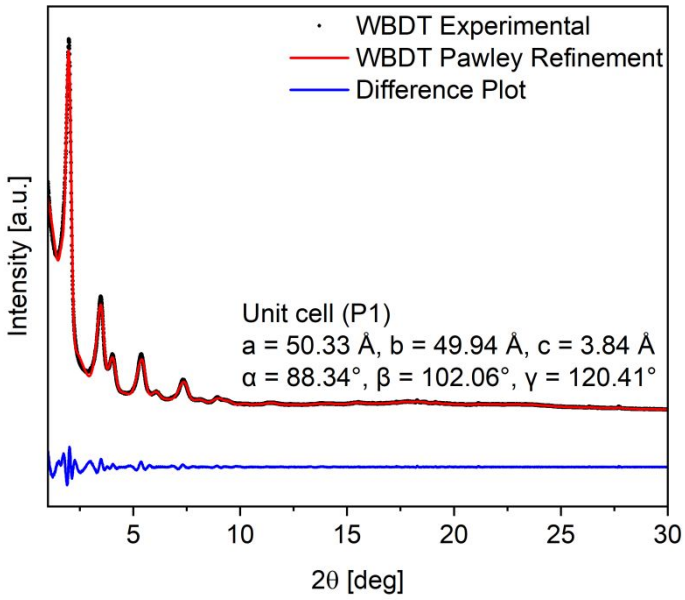

Figure S1. Experimental PXRD of the WBDT COF powder together with the Pawley refinement and the resulting difference plot. Unit cell lengths and angles are indicated.

FTIR measurements confirm the successful formation of the COF network by the disappearance of the -NH (3342 cm^{-1}) and -CO (1664 cm^{-1}) vibrational modes and the appearance of the vibrational mode of the imine bond (1609 cm^{-1}) in the IR spectrum of the WBDT COF (**Figure S2**).

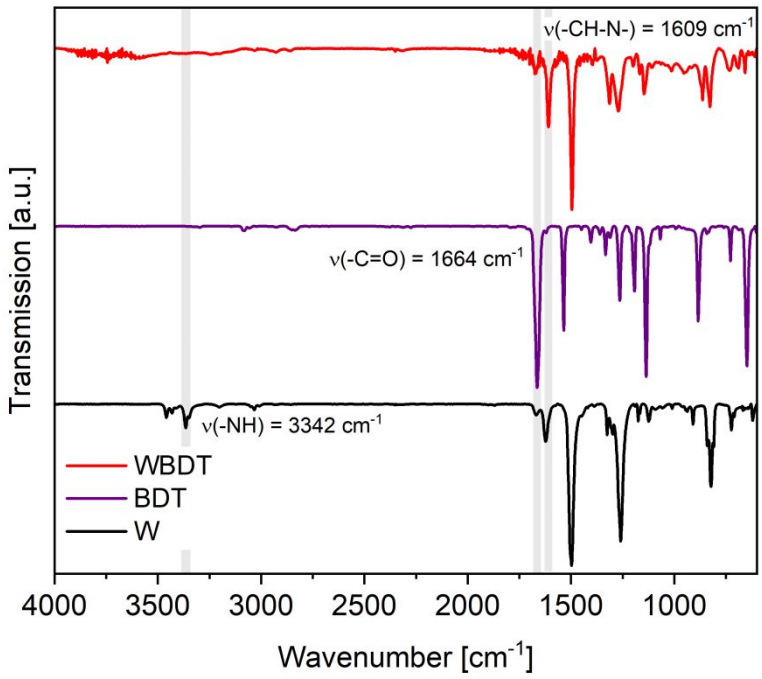

Figure S2. FTIR spectra of the two linker molecules W and BDT and of the WBDT COF.

Surface area and pore sizes of the WBDT COF were determined by nitrogen sorption measurements. The sorption isotherm is a mixture of type I and type IVb with two nitrogen uptake steps. The first step at low partial pressures is characteristic for microporous materials, whilst the second step reveals additional capillary condensation, typical for the presence of mesopores. The calculated Brunauer-Emmet-Teller surface area is 635 m^2 g^{-1} and the two pore sizes of the Kagomé-like structure, are 1.9 nm and 3.4 nm (**Figure S3**).

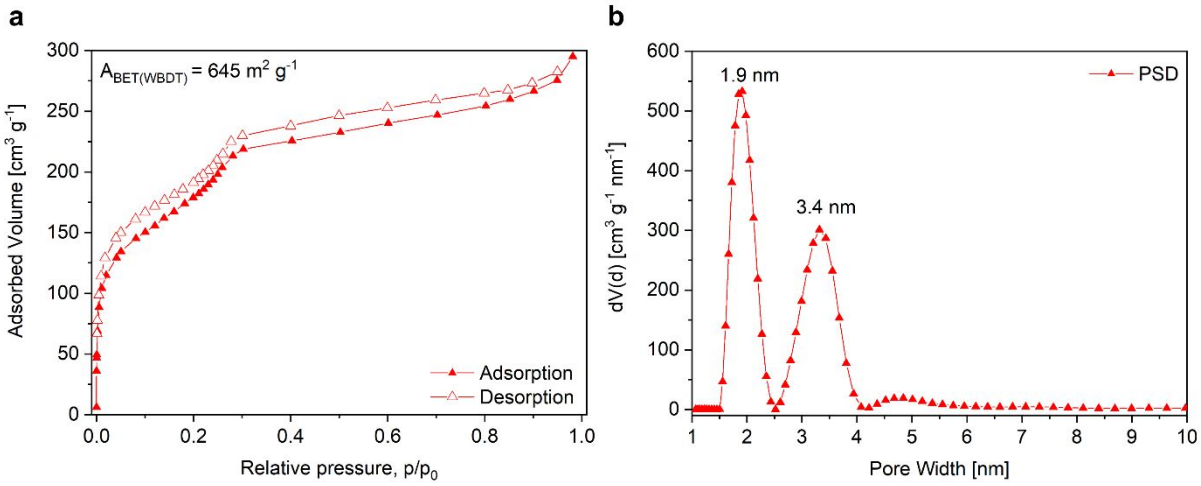

Figure S3. (**a**) Sorption isotherm of the WBDT COF with a BET surface area of 645 cm^2 g^{-1}. (**b**) Pore size distribution (PSD) with two pore sizes, 1.9 nm and 3.4 nm, consistent with the dual-pore framework of the Kagomé-like structure.

Steady-state PL and UV-Vis spectroscopy measurements were conducted to optically characterize the WBDT COF powder. The dark red COF powder emits around 1.83 eV (677 nm) and has a maximum absorption at 2.41 eV (514 nm). Fitting of the absorption onset using Tauc plot gives a direct band gap of 1.98 eV (**Figure S4**).

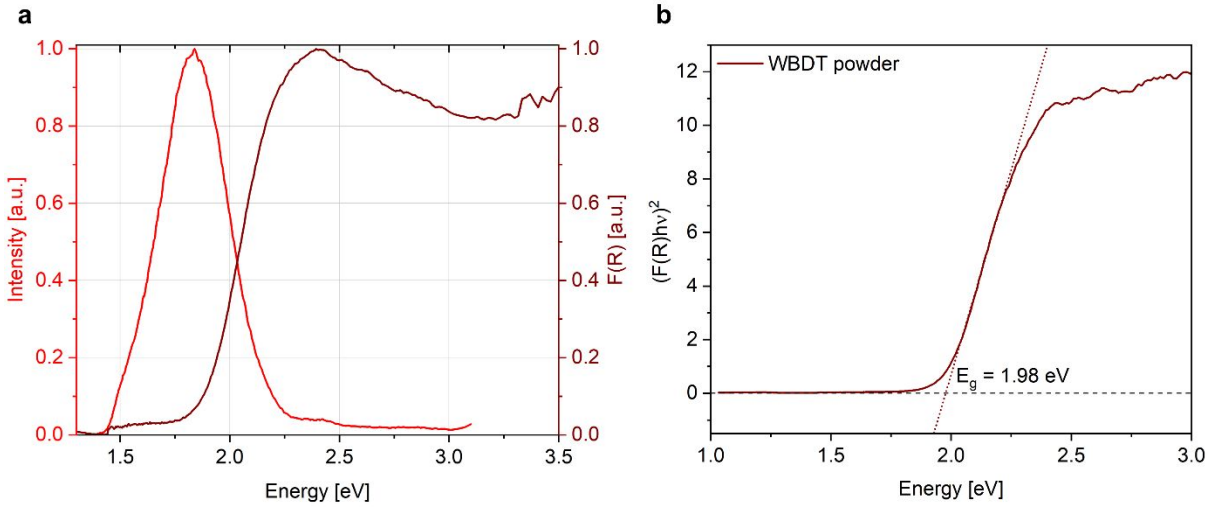

Figure S4. (**a**) Steady-state PL and UV-Vis spectra (Kubelka-Munk, diffuse reflection) of the WBDT COF powder. (**b**) Fitting of the absorption onset using Tauc plot.

Scanning electron micrographs reveal a uniform, spherical morphology of the WBDT COF particles. Transmission electron microscopy confirms the crystallinity of the COF. Detection of crystal domains with the *z*-axis oriented parallel to the incident electron beam show the pseudo-hexagonal pattern generated by the dual-pore Kagomé-like structure (**Figure S5**).

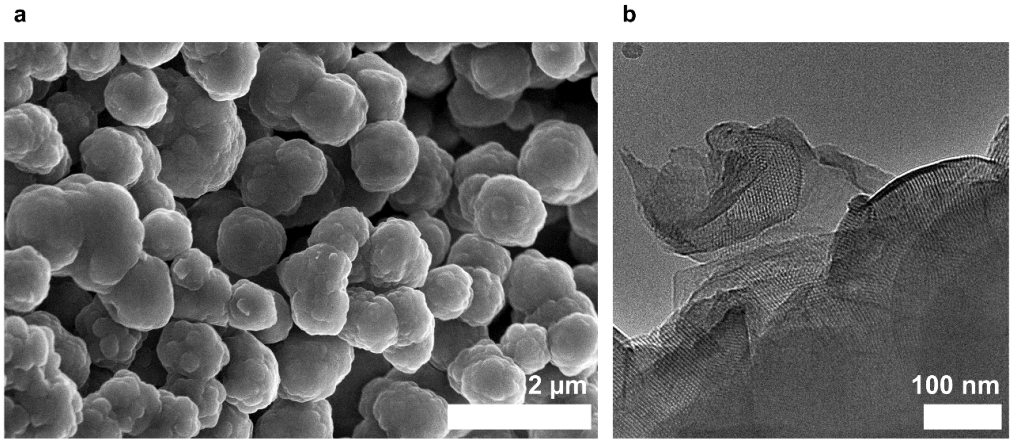

Figure S5. (**a**) SEM micrograph visualizing the spherical morphology of the WBDT COF powder. (**b**) TEM image confirming the crystalline nature of the COF.

S4. WBDT thin film characterization

Fitting of the absorption onset of the WBDT COF thin film using a Tauc plot gives a direct band gap of 2.16 eV as indicated in **Figure S6**a.

No significant broadening of the PL spectrum is visible upon decrease of the temperature. This is illustrated in **Figure S6**b, depicting the PL spectrum of the thin film at 5 K and at 300 K.

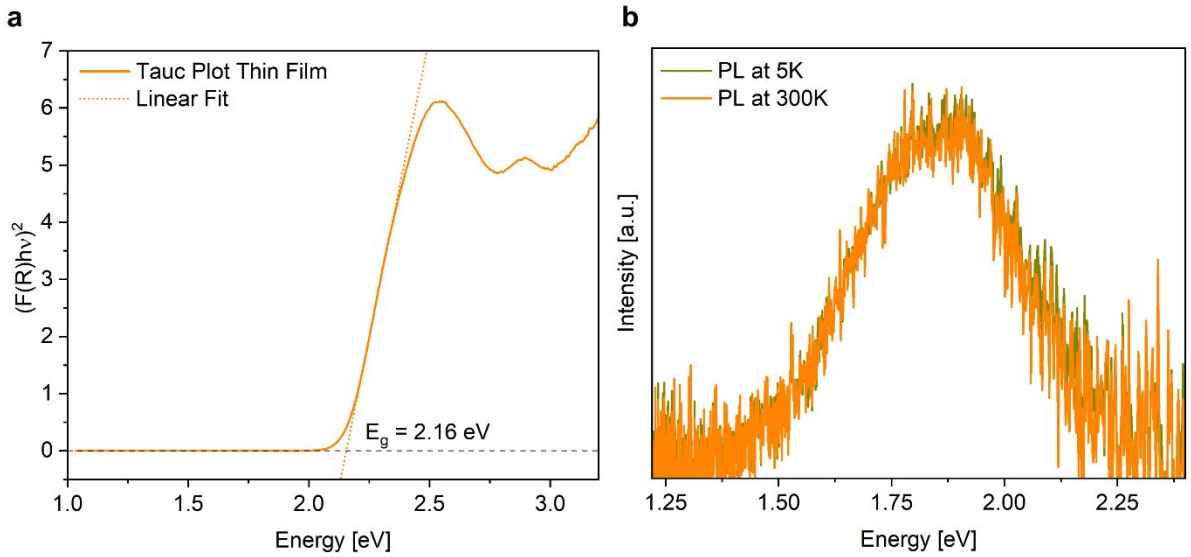

Figure S6. (**a**) Fitting of the absorption onset of the WBDT COF thin film using Tauc plot for a direct transition. (**b**) PL spectra of the thin film at 5 K and 300 K.

The thickness of the COF film was determined *via* SEM cross-section analysis (~120 nm) as well as by scanning over a thin scratch on the film's surface using AFM (~130 nm) (**Figure S7**).

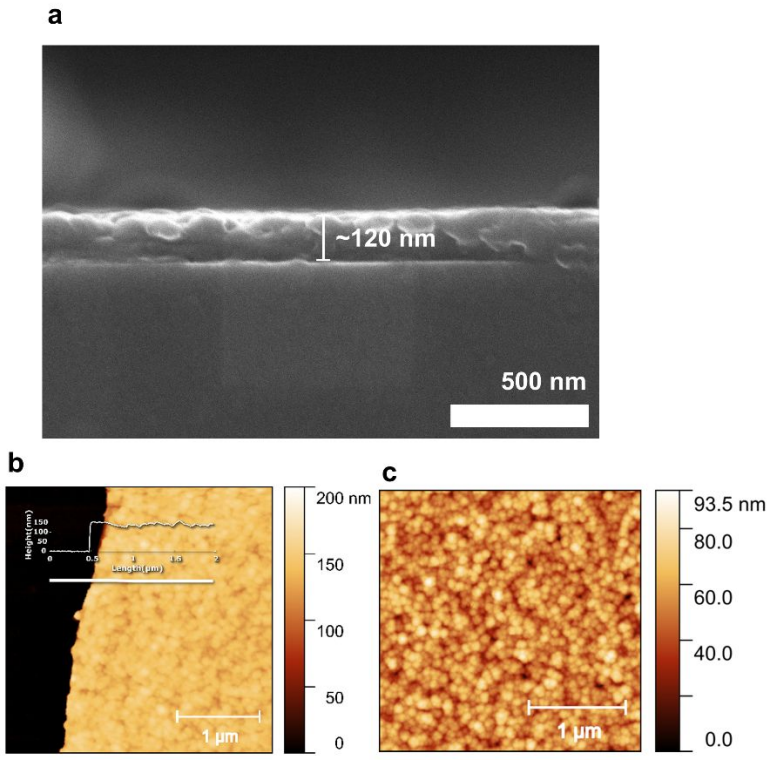

Figure S7. (**a**) SEM cross-section of the WBDT COF thin film. (**b**) AFM image of the measured scratch with the difference in height shown as inset. (**c**) AFM image of a 2.5 x 2.5 µm^2 section of the film surface.

Linear Power Dependency. For the steady-state PL and RDTR PL measurements, it is crucial that the response to the incident laser power is linear in the range of the used laser power, assuring that the number of excited states *n* is proportional to the measured intensity. **Figure S8** confirms the linear power dependency of the PL intensity up to ~50 µJ/cm^2. In order to guarantee the stability of the WBDT COF throughout the optical measurements, the laser power was chosen accordingly (see green range in **Figure S8**). All RDTR PL measurements were performed under vacuum, steady-state PL was performed under argon atmosphere.

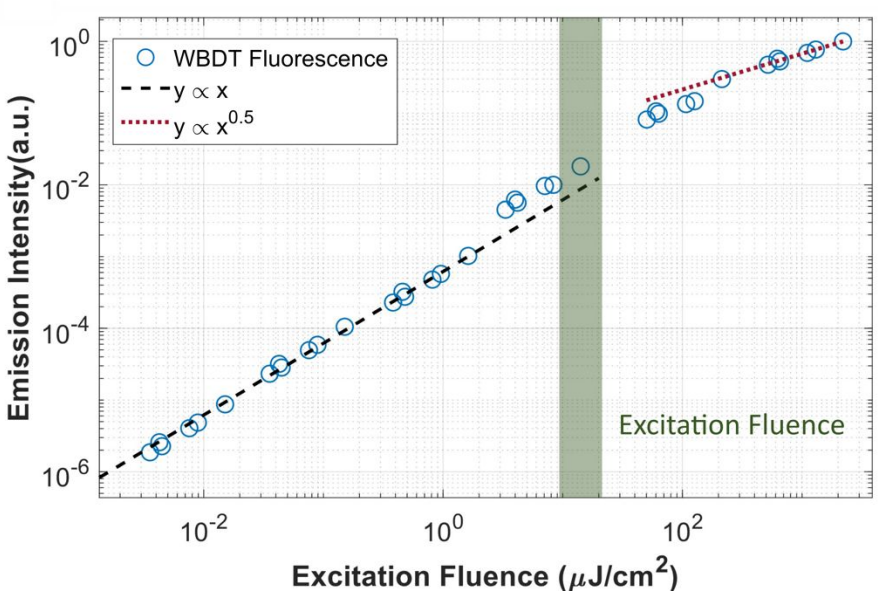

Figure S8. The excitation fluence dependency of the PL intensity. The green range shows the excitation fluence used in the experiments

Confocal Scan and Hyperspectral Images. To confirm the homogeneity of the spectral response from the thin film, confocal scanning and hyperspectral imaging of a 10 x 10 µm^2 section of the WBDT thin film were conducted, showing negligible changes in normalized intensity, central energy and spectral width of the PL signal (**Figure S9**a, b and c, respectively).

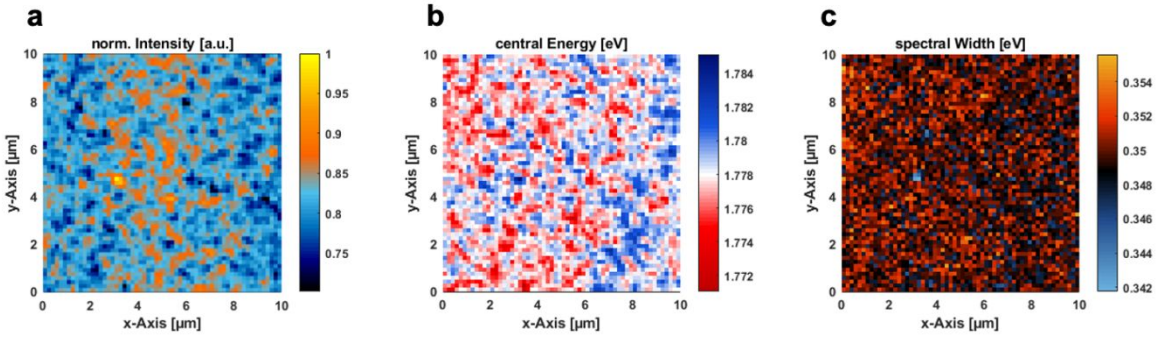

Figure S9. Confocal scan and hyperspectral images of the WBDT thin film, mapping differences in (**a**) normalized intensity, (**b**) central energy and (**c**) spectral width of the PL signal, respectively.

S5. RDTR PL measurements – Analysis and Fitting

Rayleigh length

The Rayleigh length is the distance along the beam's propagation direction from the beam waist to the point where the beam's cross-sectional area has doubled. The Rayleigh length z_R is given by [4]

$$z_R = \frac{\pi r_0^2}{\lambda}$$

where r_0 is the resolution of the confocal microscope:

$$r_0 = \frac{1.22\,\lambda}{NA}$$

With $\lambda \approx$ 500 nm and $NA =$ 0.75, a Rayleigh length of approx. 4 µm is calculated. The Rayleigh length is an order of magnitude larger than the thickness of the WBDT thin film (around 120 nm), meaning that the focused beam extends beyond the entire film thickness. As a result, the laser uniformly excites the material throughout the film thickness, ensuring that the excitation reaches the entire depth of the film simultaneously. The observed diffusion is therefore treated as a two-dimensional process.

Analysis and Fitting

The data were collected in the form of a TCSPC transient for every remote position of the tiltable mirror. For each temperature step, transients from two different directions through the confocal spot were recorded. Furthermore, two temperature series were measured to guarantee the reproducibility of the observed diffusive transport. Data set 1 was integrated over the blue part of the PL spectrum (590-610 nm, 2.03 – 2.10 eV) and Data Set 2 was integrated over the whole PL signal. In both sets the same trend of the diffusive transport was observed. Since the spectrum contains not only mobile species but also a localized radiative state, the diffusive transport is more visible in the blue data set (Data Set 1). An exemplary data set at 40 K is shown in **Figure S10**:

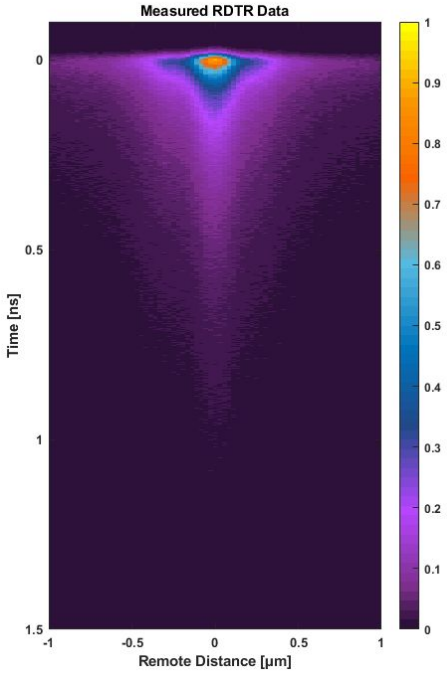

Figure S10. RDTR PL data obtained at 40 K.

As the COF film is thin (~ 100 nm), and the Rayleigh length is around a micrometer, the focus penetrates the whole film in the direction perpendicular to the substrate (*z*-direction). This measuring setup only allows for the observation of the in-plane 2D diffusive transport in the thin film (although this does not exclude occasional transport along *z* followed by in-plane (*xy*) transport).

The observed diffusive species has a limited lifetime, leading us to the following differential equation (S1):

$$\frac{dn(x,y,t)}{dt} = D\Delta n(x,y,t) - k_1 n(x,y,t) \qquad \text{(S1)}$$

In equation S1, n is the number of excited states that is proportional to the measured PL intensity. This is confirmed by linear power dependency (**Figure S8**). D is the diffusion coefficient and k_1 is the lifetime of the diffusive species. Assuming a Gaussian starting distribution of excited states, this differential equation can be analytically solved by

$$n(x,y,t) = \frac{N_0 2\sigma^2}{2\sigma^2+4Dt} exp\left(\frac{-x^2-y^2}{2\sigma^2+4Dt}\right) \cdot \exp\left(-k_1 t\right), \tag{S2}$$

where the spatial integration over $N_0\, exp\left(\frac{-x^2-y^2}{2\sigma^2}\right)$ is the total number of excited states at $t = 0$ and σ is the width of the starting Gaussian distribution. To analyse the RDTR PL data, two different methods were used and subsequently compared for cross-verification. For the first method (method I in the main text), we fit two Gaussians, one with a fixed width corresponding to the initial signal width determined by the excitation focus and the optical resolution of the setup and the other with a variable width (**Figure S11**a). The results show that the variance of the width σ^2 follows a linear change in time, as expected from the following relation (equation S3), derived from the 2D diffusion equation S2:

$$\sigma^2 \sim 2Dt \tag{S3}$$

This linear relation is shown in **Figure S11**b. The contribution with fixed (time-independent) width is attributed to a localized, immobile excited species, presumably related to defect trap states.

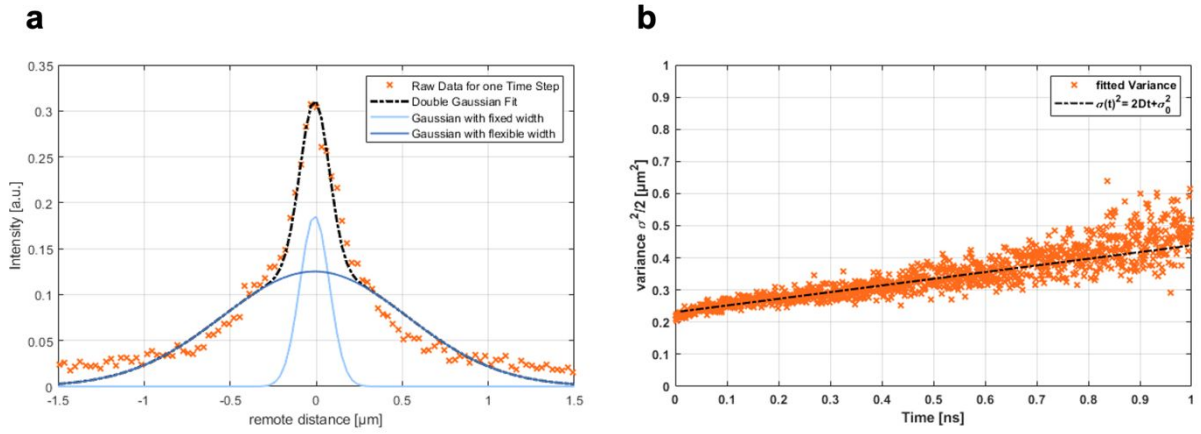

Figure S11. (**a**) Double Gaussian fit (fixed and flexible width) of the raw RDTR PL data for one time step. (**b**) Linear fit of the variance of the width as a function of time.

The second method (method II in the main text) involves analysing the full data set using the analytical solution (equation S2) and fitting the whole two-dimensional data with a single diffusion coefficient. This analysis is split into two parts according to the two different timescales observed (*fast* and *slow*

species, **Figure 3b**). **Figure S12** visualizes and compares the diffusion coefficients obtained by the two methods for the *slow species*.

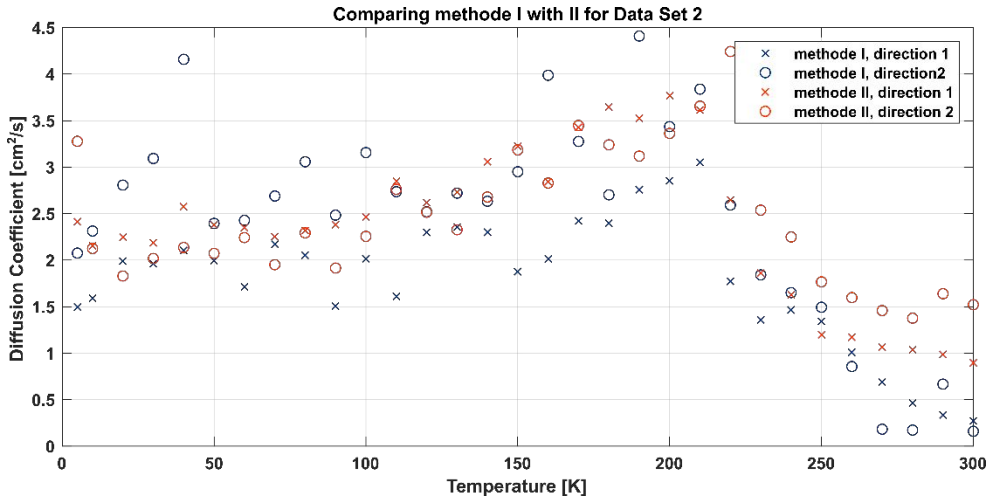

Figure S12. Comparison of the two methods I and II for the determination of the diffusion coefficient *D* for data set 2 (full spectral range). Data are collected in two different scanning directions through the confocal spot, perpendicular to each other (direction 1 and 2).

For the free charge carrier diffusion coefficient, the time interval from -0.025 to 0.005 ns is used. Additionally, the calculated data are convoluted with the instrument response function (IRF, FWHM of 28 ps). The time-zero is defined by the maximum and the overlap of the initial rise of the IRF at the center of the confocal spot (remote distance = 0 µm). An additional Gauss distribution with a mono-exponential decay is added, representing the localized excited states.

For the free charge carrier diffusion, only method I was used, and the data were averaged over both directions (**Figure S13**a). The time interval between 0.1 and 1 ns was used for the exciton diffusion coefficient. Here, both methods I and II were applied, and the data were averaged over both directions (**Figure S13**b).

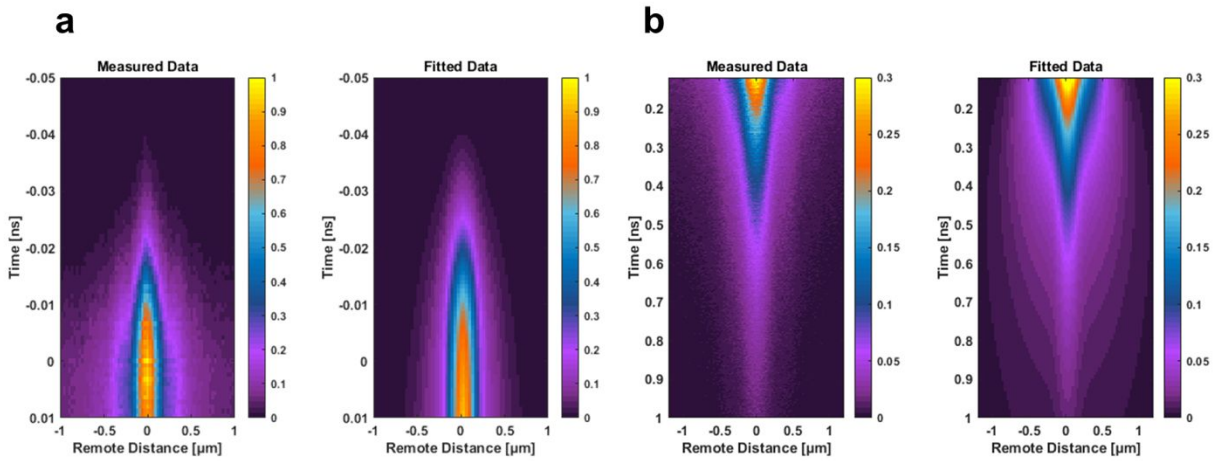

Figure S13. Measured and fitted data for the diffusion coefficient of the (**a**) free charge carriers and (**b**) excitons.

According to the fits, the lifetimes τ of the excitons are at the order of 0.9 - 1.2 ns. Using τ, the diffusion length L_D can be approximated:

$$L_D = \sqrt{2D\tau} \tag{S4}$$

The diffusion length of the excitons as a function of temperature is depicted in **Figure S14**.

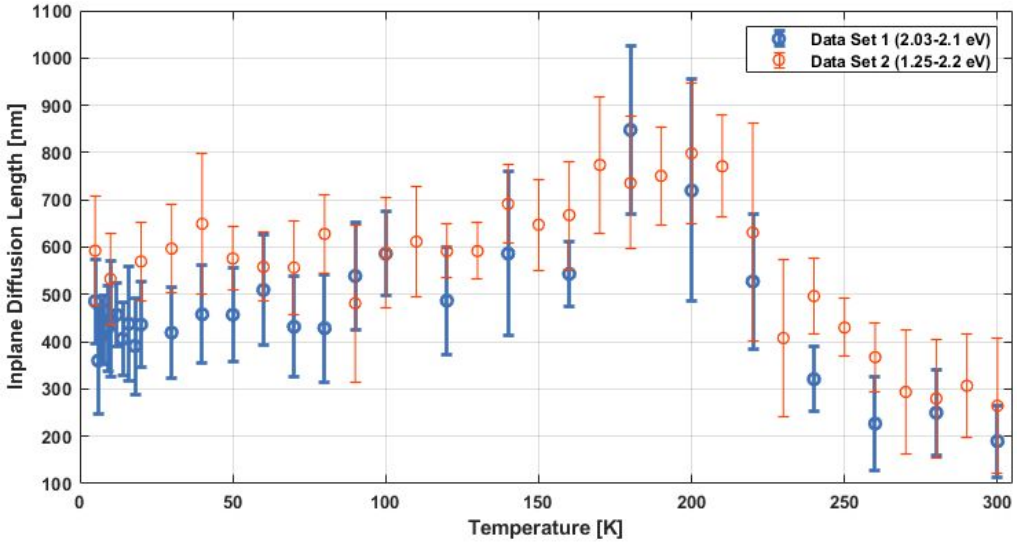

Figure S14. Diffusion length of the excitons as a function of temperature.

S6. WBDT un-oriented thin film characterization and diffusion dynamics

Characterization

The WBDT COF has a strong tendency to grow highly oriented thin films on most substrates, even when incorrect ratios of building blocks are used or different solvents are chosen for the COF synthesis. Therefore, we changed the substrate's morphology drastically from a smooth surface to a meso-structured SiO_2 inverse opal with a thickness of ~ 4 µm and pores of 300 nm diameter. On this substrate, WBDT COF grows as interconnected spherical grains of around 150-200 nm size similar to the bulk powder, both in and on top of the structure. **Figure S15**a and b show SEM top views of the inverse opal structure, and c and d show the WBDT COF@SiO_2 grown on top the macro-structured substrate.

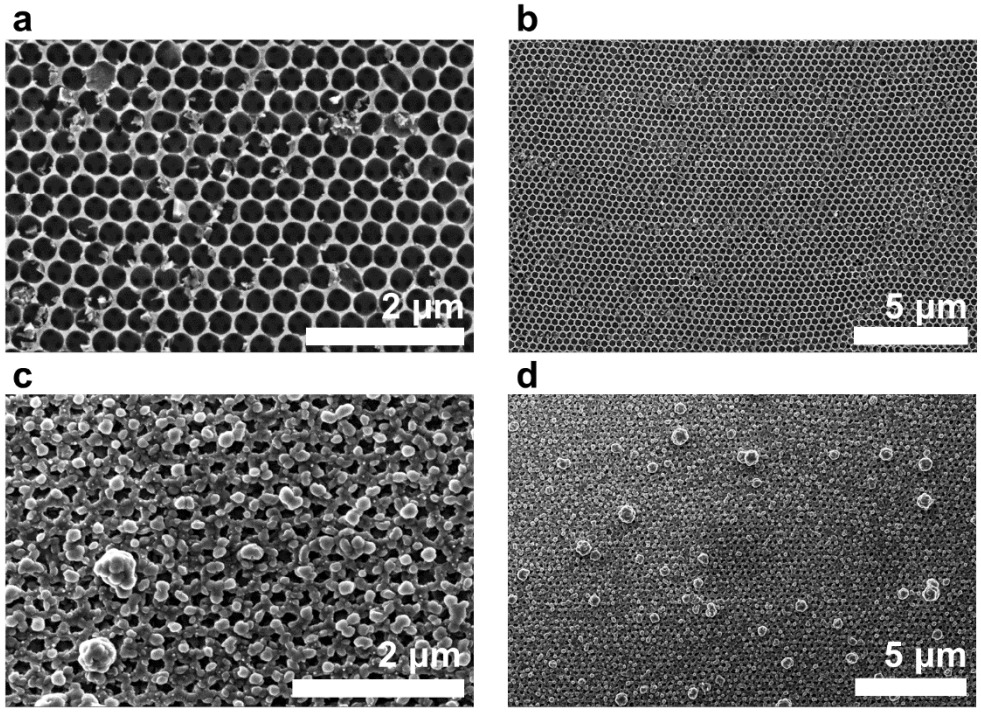

Figure S15. (**a**) and (**b**) Top view of the SiO_2 inverse opal structure at different magnifications. (**c**) and (**d**) WBDT COF@SiO_2 inverse opal structure.

Figure S16a and c show cross sections of the WBDT COF@SiO_2, illustrating the COF growth both into the mesopores and on top of the structure. Figure b and d show the same section of the film, looking only at the backscattered electrons. This method has a higher contrast for the inorganic SiO_2, revealing the SiO_2 structure below the COF grains.

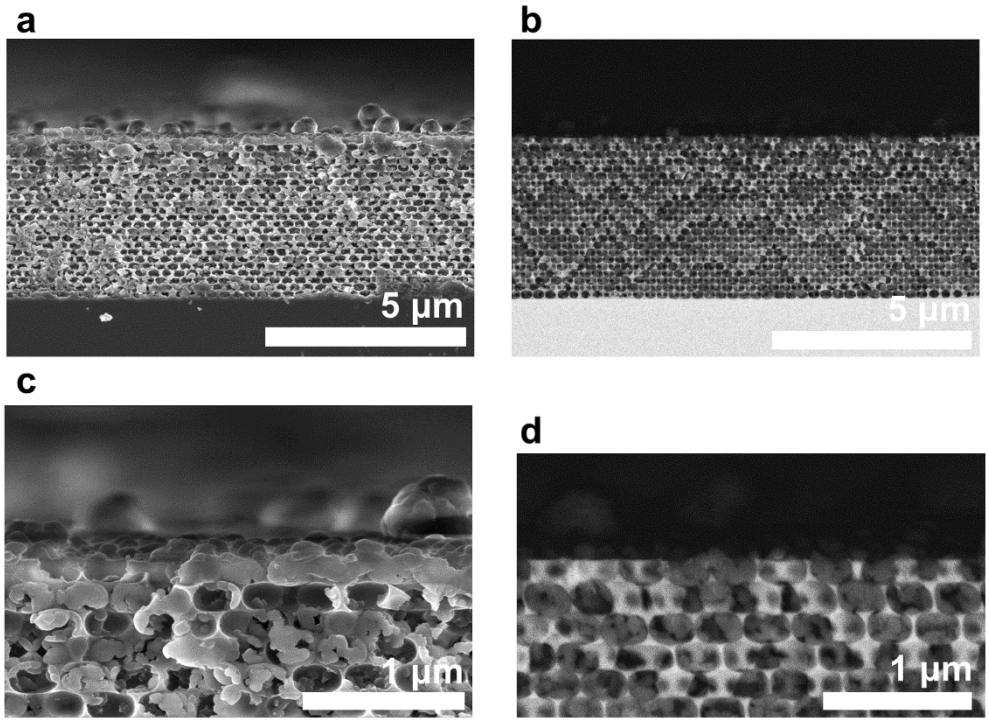

Figure S16. (**a**) and (**c**) Cross section of WBDT COF@SiO_2 with different magnifications, showing the growth of the COF both into the structure as well as on top of it. (**b**) and (**d**) Backscattered electron image of the same film sections as in (**a**) and (**c**), revealing the SiO_2 structure below the COF.

Additionally, AFM was conducted on a 2.5 x 2.5 µm^2 section of the un-oriented thin film to better illustrate the difference in morphology compared to the oriented WBDT film (**Figure S17**)

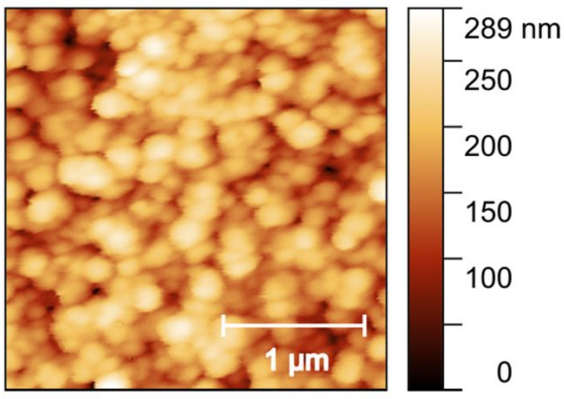

Figure S17. AFM image of a 2.5 x 2.5 µm^2 section of the un-oriented WBDT thin film.

In **Figure S18**, the reflections in the GIWAXS pattern of the un-oriented film appear at identical scattering vectors in the GIWAXS pattern of the oriented film and in the PXRD pattern of the bulk material, confirming the formation of a crystalline COF. The intensity of the *hkl* reflections is uniformly distributed in q_z and q_r direction, forming a semi-circle. The scattering pattern indicates a random orientation of the COF crystallites.

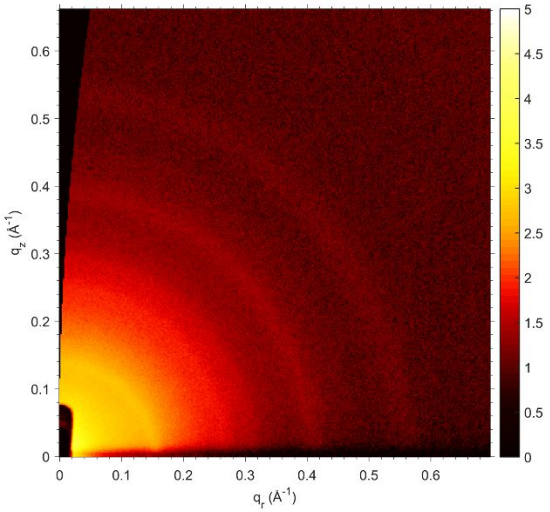

Figure S18. GIWAXS pattern of the un-oriented WBDT COF grown on an SiO_2 inverse opal structure. The colour map was chosen differently to the main text to improve the visibility of the reflections at low q_r values.

Steady-state PL and UV-Vis measurements were conducted to optically characterize the WBDT COF@SiO_2 film. The dark red film emits at 1.88 eV (660 nm) and has a maximum absorption at 2.48 eV (500 nm). Fitting of the absorption onset using Tauc plot gives a direct band gap of 2.08 eV (**Figure S19**)

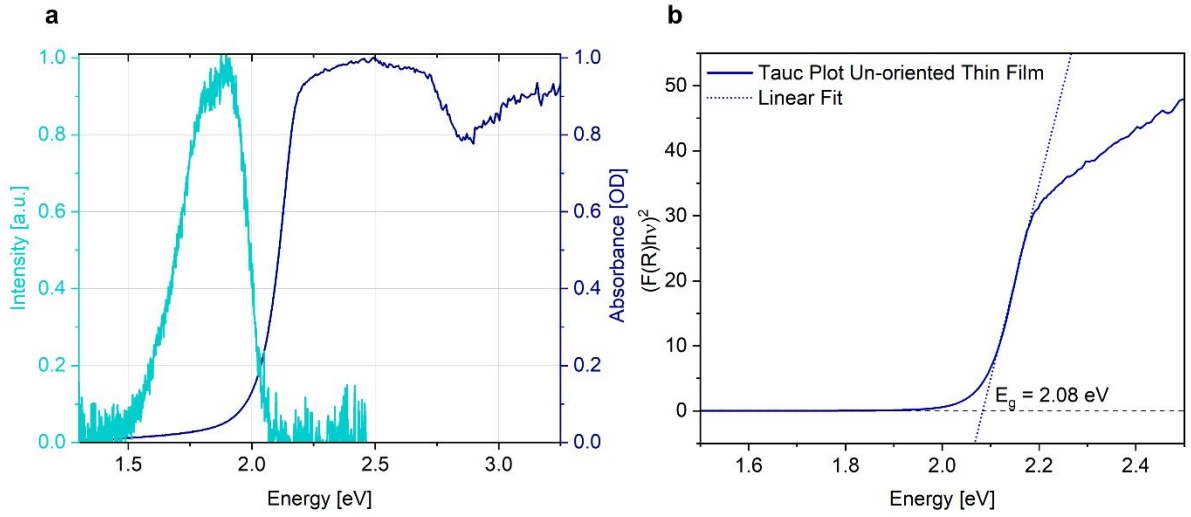

Figure S19. (**a**) Steady-state PL and UV-Vis spectra of the unoriented WBDT COF thin film. (**b**) Tauc plot of the absorption onset, scaled for a direct transition.

Diffusion Dynamics

The analysed RDTR PL data for the un-oriented WBDT COF thin film are shown in **Figure S20**. With $D_{unoriented} \approx 11$ cm^2 s^{-1}, the diffusion coefficient for the free charge carriers at the shorter timescale is comparable to that of the oriented thin film ($D_{oriented} = 10$ cm^2 s^{-1}). This is in line with our interpretation of the carriers diffusing within one grain and the grain size not significantly changing between oriented and un-oriented film. The exciton diffusion coefficient decreases with decreasing temperature, indicating a *hopping* type transport. It is also overall lower, suggesting that the high degree of orientation of the crystallites in the oriented film plays a major role in the diffusive transport.

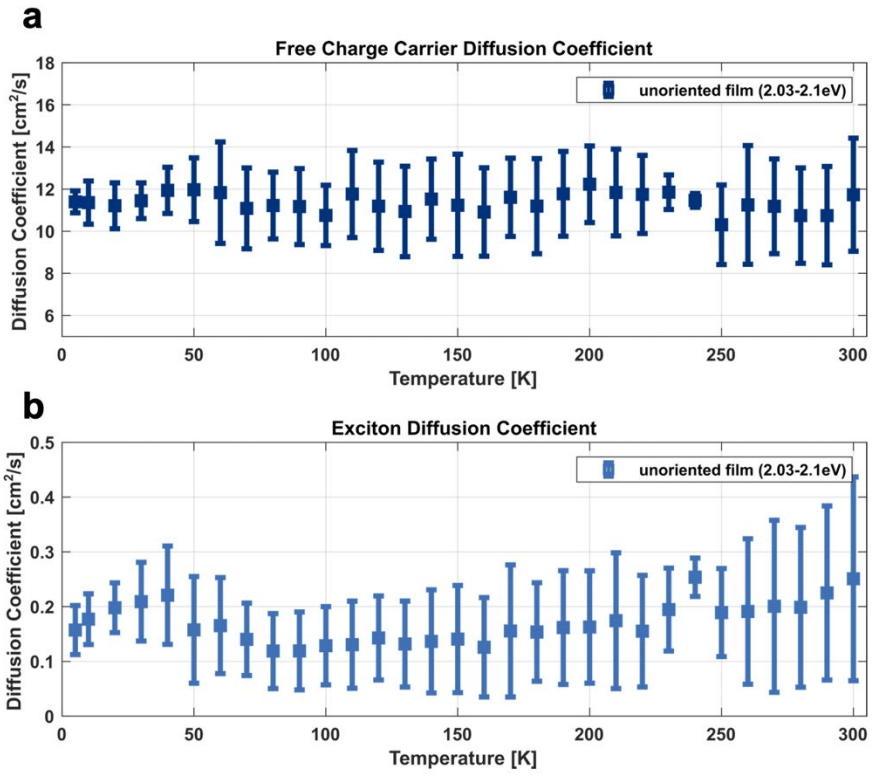

Figure S20. Diffusion coefficient as a function of temperature of the (**a**) free charge carriers and (**b**) excitons in the un-oriented WBDT COF thin film.

S7. Optical Pump Terahertz Probe Spectroscopy (OPTP)

The setup used for optical pump terahertz probe (OPTP) transients is described in full detail elsewhere.[5] Briefly, an amplified Ti:sapphire laser system (Spitfire ACE, Spectra-Physics) provides 800-nm light pulses (35 fs) with 5-kHz repetition rate. The fundamental output of the amplified Ti:sapphire laser is used to generate single-cycle THz radiation pulses in a W/$Co_{40}Fe_{40}B_{20}$/Pt multilayer film on quartz (spintronic emitter) through the inverse spin Hall effect.[6] Furthermore, the optical excitation pulses (400 nm) used to photoexcite the samples are generated by second-harmonic generation in a beta-barium-borate (BBO) crystal. During OPTP measurements, the fractional changes in the THz transmission (0.5-2.5 THz) following the 400-nm photoexcitation are monitored by using free-space electro-optic sampling (EOS) in a 1-mm-thick (110)-ZnTe crystal. The WBDT COF thin films were deposited onto 2 mm thick z-cut quartz. During OPTP measurements, the THz emission and detection optics and samples are kept under vacuum at pressures below 0.1 mbar.

Extraction of charge-carrier mobility from OPTP measurements

We extracted the effective charge-carrier mobility following the method developed by Wehrenfennig et al..[7] Briefly, for semiconductor thin films materials with thicknesses smaller than the wavelength of the incident THz radiation, the sheet photoconductivity can be estimated from the fractional change in the transmitted THz electric field $\Delta T/T$, and expressed as

$$\Delta S = -\epsilon_0 c(n_q + n_v)\left(\frac{\Delta T}{T}\right) \tag{S6}$$

where n_q = 2.13 and n_v = 1 are the refractive indexes of quartz and vacuum, respectively.[8]

To extract the effective charge-carrier mobility from the sheet photoconductivity, the number of initially photogenerated carriers is estimated as

$$N = \phi \frac{E\lambda}{hc}\left(1 - R_p - T_p\right) \tag{S7}$$

Where φ is the photon-to-charge branching ratio (i.e., the fraction of generated charges per photon absorbed), E is the pump pulse energy, λ is the excitation wavelength, and R_p and T_p are the reflectance and transmittance of the sample at the excitation wavelength (3.1 eV, 400 nm). The charge-carrier mobility μ can be calculated as

$$\mu = \frac{\Delta S\, A_{eff}}{Ne} \tag{S8}$$

Where A_{eff} is the effective overlap area between THz and pump beam and e is the elementary charge. By substituting Equation S6 and Equation S7 into Equation S8, the effective charge-carrier mobility is obtained as:

$$\varphi\mu = -\epsilon_0 c(n_q + n_v)\frac{A_{eff}hc}{eE\lambda(1 - R_{pump} - T_{pump})}\left(\frac{\Delta T}{T}\right) \quad \text{(S9)}$$

Here, it is worth noting that the sheet photoconductivity signal measured by OPTP arises from the contributions of both photogenerated free electrons and holes. Therefore, the extracted charge-carrier mobility is the effective electron-hole sum mobility.

Calculation of the diffusion length using charge carrier lifetime from OPTP

In this study, we calculated the diffusion length L_D of the free charge carriers (*fast species*) using the lifetime extracted from OPTP measurements τ = 1.4 ps and the diffusion coefficient given by RDTR PL $D \sim 10$ cm^2 s^{-1}, assuming that the fast-moving species are equal to the free charge carriers. Both methods are independent and generate two different values. OPTP measures only the free charge carriers, formed shortly after excitation. From the absorbed probe signal, an effective mobility is calculated and a lifetime of the free charge carriers can be extracted. The effective mobility $\varphi\mu \sim 0.12 \pm 0.05\ cm^2V^{-1}s^{-1}$contains the photon-to-charge branching ratio φ, since the exact number of contributing free charge carriers is unknown. In RDTR PL measurements however, the PL is generated by a combination of free charge carriers and possible unbound excitons. Here, the diffusive transport is only driven by the chemical potential of the generated excited states, while in OPTP measurements, the excited charge carriers react to the applied THz probing field.

In principle the absolute mobility μ and diffusion coefficient D can be connected *via* the Einstein-Smoluchowski[9,10] relation:

$$D = \frac{\mu k_B T}{e} \quad \text{(S10)}$$

with the Boltzmann constant k_B, the temperature T and the elemental charge e. However, this formula is only valid in the case of a charged particle with a charge e, moving through a neutral medium. In our case, the excited charges are bound to each other (exciton) or move as ambipolar charge carriers (combined movement of electrons and holes) in a dielectric and periodic crystal lattice. This lattice shields the charges. Therefore, the Einstein-Smoluchowski relation cannot be readily applied here. A more accurate model would be needed to contextualize both numbers. Additionally, it is not clear if the disorder in the system has an influence on the fast-moving species.

Hence, the calculated diffusion length of the free charge carriers (*fast species*) in this study, combining values from both OPTP and RDTR PL measurements, should be considered as a qualitative estimation.

S8. Theoretical Calculations

The structure of WBDT is optimized at density functional theory (DFT) level. We use the projector-augmented wave (PAW) method[11,12] in conjugation with Perdew-Burke-Ernzerhof (PBE) exchange and correlation functional[13] as implemented in the Vienna ab-initio simulation package (VASP).[14–16] The atomic positions are relaxed using the conjugate gradient method with an energy convergence value of 10^{-6} eV. The dispersion interactions are described with the nonlocal vdW-DF functionals by Dion et al.[17] The band structure of WBDT shown in Figure 2a has been corrected by a scissors shift[18] of +0.49 eV for all conduction bands to estimate the band gap at Hybrid-DFT (HSE06) level (L. Fuchs et al. unpublished).

The Brillouin zone (BZ) for the relaxation simulations is sampled with a 1x1x6 Γ-centered mesh. The electronic band structure (**Figure 2a**) is calculated along a path connecting high-symmetry points in the primitive hexagonal cell (Γ-M-K-Γ-A) with 20 equally spaced points between two special points. Additionally, atomic projections of the Kohn-Sham states onto W and BDT fragments were calculated.

For the calculation of the transition densities of the excited states, WBDT is divided into two precursor fragments (BDT and W), which are NH- and H-terminal saturated. After a gas phase relaxation of the fragments with VASP, the transition densities describing the excited states are calculated with the software gaussian16[19] and Multiwfn,[20] using M062X as the exchange-correlation functional and a cc-pVTZ basis set. Excitonic transition densities are used to calculate the Coulomb interaction between the exciton states that are placed at the fragment position in the COF as described earlier[21] with an effective screening described by a low relative dielectric permittivity of $\epsilon = 2$. The large electron and hole transfer integrals extracted from the calculated band structure are further taken into account for second-order transfer processes to estimate the resulting effective exciton transfer integrals of $\varepsilon \cong 50$ meV.

A Marcus-type hopping ansatz with exciton coupling of $\varepsilon \cong 50$ meV and an estimated reduced reorganization energy of $\Lambda \cong 0.1$ eV was used to estimate the diffusion coefficient at 300 K.

References

(1) Sick, T.; Rotter, J. M.; Reuter, S.; Kandambeth, S.; Bach, N. N.; Döblinger, M.; Merz, J.; Clark, T.; Marder, T. B.; Bein, T.; Medina, D. D. Switching on and off Interlayer Correlations and Porosity in 2D Covalent Organic Frameworks. *J. Am. Chem. Soc.* **2019**, *141* (32), 12570–12581. DOI: 10.1021/jacs.9b02800. Published Online: Feb. 8, 2019.

(2) Rotter, J. M.; Guntermann, R.; Auth, M.; Mähringer, A.; Sperlich, A.; Dyakonov, V.; Medina, D. D.; Bein, T. Highly conducting Wurster-type twisted covalent organic frameworks. *Chem. Sci.* **2020**, *11* (47), 12843–12853. DOI: 10.1039/d0sc03909h. Published Online: Oct. 27, 2020.

(3) Hatton, B.; Mishchenko, L.; Davis, S.; Sandhage, K. H.; Aizenberg, J. Assembly of large-area, highly ordered, crack-free inverse opal films. *PNAS* **2010**, *107* (23), 10354–10359. DOI: 10.1073/pnas.1000954107. Published Online: May. 19, 2010.

(4) Zinth, W.; Zinth, U. *Optik : Lichtstrahlen - Wellen - Photonen / Wolfgang Zinth, Ursula Zinth*; Oldenbourg Wissenschaftsverlag, 2011.

(5) Buizza, L. R. V.; Wright, A. D.; Longo, G.; Sansom, H. C.; Xia, C. Q.; Rosseinsky, M. J.; Johnston, M. B.; Snaith, H. J.; Herz, L. M. Charge-Carrier Mobility and Localization in Semiconducting Cu2AgBiI6 for Photovoltaic Applications. *ACS Energy Lett.* **2021**, *6* (5), 1729–1739. DOI: 10.1021/acsenergylett.1c00458. Published Online: Apr. 7, 2021.

(6) Seifert, T.; Jaiswal, S.; Martens, U.; Hannegan, J.; Braun, L.; Maldonado, P.; Freimuth, F.; Kronenberg, A.; Henrizi, J.; Radu, I.; Beaurepaire, E.; Mokrousov, Y.; Oppeneer, P. M.; Jourdan, M.; Jakob, G.; Turchinovich, D.; Hayden, L. M.; Wolf, M.; Münzenberg, M.; Kläui, M.; Kampfrath, T. Efficient metallic spintronic emitters of ultrabroadband terahertz radiation. *Nat. Photonics* **2016**, *10* (7), 483–488. DOI: 10.1038/nphoton.2016.91.

(7) Wehrenfennig, C.; Eperon, G. E.; Johnston, M. B.; Snaith, H. J.; Herz, L. M. High charge carrier mobilities and lifetimes in organolead trihalide perovskites. *Adv. Mater.* **2014**, *26* (10), 1584–1589. DOI: 10.1002/adma.201305172.

(8) Joyce, H. J.; Boland, J. L.; Davies, C. L.; Baig, S. A.; Johnston, M. B. A review of the electrical properties of semiconductor nanowires: insights gained from terahertz conductivity spectroscopy. *Semicond. Sci. Technol.* **2016**, *31* (10), 103003. DOI: 10.1088/0268-1242/31/10/103003.

(9) Einstein, A. Über die von der molekularkinetischen Theorie der Wärme geforderte Bewegung von in ruhenden Flüssigkeiten suspendierten Teilchen. *Ann. Phys.* **1905**, *322* (8), 549–560. DOI: 10.1002/andp.19053220806.

(10) Smoluchowski, M. von. Zur kinetischen Theorie der Brownschen Molekularbewegung und der Suspensionen. *Ann. Phys.* **1906**, *326* (14), 756–780. DOI: 10.1002/andp.19063261405.

(11) Blöchl, P. E. Projector augmented-wave method. *Phys Rev B Condens Matter* **1994**, *50* (24), 17953–17979. DOI: 10.1103/physrevb.50.17953.

(12) Kresse, G.; Joubert, D. From ultrasoft pseudopotentials to the projector augmented-wave method. *Phys. Rev. B* **1999**, *59* (3), 1758–1775. DOI: 10.1103/physrevb.59.1758.

(13) Perdew, J. P.; Burke, K.; Ernzerhof, M. Generalized Gradient Approximation Made Simple. *Phys. Rev. Lett.* **1996**, *77* (18), 3865–3868. DOI: 10.1103/physrevlett.77.3865.

(14) Kresse, G.; Hafner, J. Ab initio molecular-dynamics simulation of the liquid-metal-amorphous-semiconductor transition in germanium. *Phys Rev B Condens Matter* **1994**, *49* (20), 14251–14269. DOI: 10.1103/physrevb.49.14251.

(15) Kresse, G.; Furthmüller, J. Efficiency of ab-initio total energy calculations for metals and semiconductors using a plane-wave basis set. *Comput. Mater. Sci* **1996**, *6* (1), 15–50. DOI: 10.1016/0927-0256(96)00008-0.

(16) Kresse, G.; Furthmüller, J. Efficient iterative schemes for ab initio total-energy calculations using a plane-wave basis set. *Phys. Rev. B* **1996**, *54* (16), 11169–11186. DOI: 10.1103/PhysRevB.54.11169.

(17) Dion, M.; Rydberg, H.; Schröder, E.; Langreth, D. C.; Lundqvist, B. I. van der Waals density functional for general geometries. *Phys. Rev. Lett.* **2004**, *92* (24), 246401. DOI: 10.1103/PhysRevLett.92.246401. Published Online: Jun. 16, 2004.

(18) Bechstedt, F. *Many-body approach to electronic excitations*:*Concepts and applications*, Vol. 181; Springer, 2015. DOI: 10.1007/978-3-662-44593-8.

(19) M. J. Frisch, G. W. Trucks, H. B. Schlegel, G. E. Scuseria, M. A. Robb, J. R. Cheeseman, G. Scalmani, V. Barone, B. Mennucci, G. A. Petersson, H. Nakatsuji, M. Caricato, X. Li, H. P. Hratchian, A. F. Izmaylov, J. Bloino, G. Zheng, J. L. Sonnenberg, M. Hada, M. Ehara, K. Toyota, R. Fukuda, J. Hasegawa, M. Ishida, T. Nakajima, Y. Honda, O. Kitao, H. Nakai, T. Vreven, J. A. Montgomery, Jr., J. E. Peralta, F. Ogliaro, M. Bearpark, J. J. Heyd, E. Brothers, K. N. Kudin, V. N. Staroverov, T. Keith, R. Kobayashi, J. Normand, K. Raghavachari, A. Rendell, J. C. Burant, S. S. Iyengar, J. Tomasi, M. Cossi, N. Rega, J. M. Millam, M. Klene, J. E. Knox, J. B. Cross, V. Bakken, C. Adamo, J. Jaramillo, R. Gomperts, R. E. Stratmann, O. Yazyev, A. J. Austin, R. Cammi, C. Pomelli, J. W. Ochterski, R. L. Martin, K. Morokuma, V. G. Zakrzewski, G. A. Voth, P. Salvador, J. J. Dannenberg, S. Dapprich, A. D. Daniels, Ö. Farkas, J. B. Foresman, J. V. Ortiz, J. Cioslowski, and D. J. Fox. *Gaussian 16, Revision B.01*; Gaussian, Inc., 2016.

(20) Lu, T.; Chen, F. Multiwfn: a multifunctional wavefunction analyzer. *Journal of computational chemistry* **2012**, *33* (5), 580–592. DOI: 10.1002/jcc.22885. Published Online: Dec. 8, 2011.

(21) Müller, K.; Schellhammer, K. S.; Gräßler, N.; Debnath, B.; Liu, F.; Krupskaya, Y.; Leo, K.; Knupfer, M.; Ortmann, F. Directed exciton transport highways in organic semiconductors. *Nat. Commun.* **2023**, *14* (1), 5599. DOI: 10.1038/s41467-023-41044-9. Published Online: Sep. 12, 2023.